



OPEN

Green synthesis and characterization of CuO/PANI nanocomposite for efficient Pb (II) adsorption from contaminated water

Hailemariam Assefa¹, Simranjeet Singh², Nabila Shehata³, Nadeem A. Khan⁴, Femi Emmanuel Olu¹✉ & Praveen C. Ramamurthy²✉

This study presents the synthesis of a green polymer-based nanocomposite by incorporating green CuO nanoparticles into polyaniline (PANI) for the adsorption of Pb (II) ions from contaminated water. The nanocomposite was extensively characterized using FTIR, XRD, BET, SEM-EDX, XPS, and Raman spectroscopy, both before and after Pb(II) adsorption. Optimization studies were performed to assess the effects of key parameters, including pH, adsorbent dosage, and initial ion concentration on the adsorption process. Adsorption isotherms and kinetic models were applied to analyze the experimental data, revealing that the Freundlich isotherm provided the best fit, with a high correlation coefficient (R^2) and a $(1/n)$ value less than 1, indicating favorable adsorption conditions. Furthermore, the Avrami and pseudo-first-order kinetic models demonstrated superior fitting compared to other models. The green nanocomposite exhibited outstanding adsorption capacity, highlighting its potential as a sustainable and efficient adsorbent for Pb(II) removal from wastewater.

Keywords Green Polymer, Nanocomposite, Pb (II) adsorption, Kinetics

In recent years, environmental pollution by heavy metals has intensified, driven by industrial production, energy consumption, mining operations, and the widespread use of pesticides and fertilizers^{1,2}. Lead (Pb), a widely prevalent and highly toxic metal, is found in various environmental ecosystems, including urban and residential areas. The discharge of lead-contaminated wastewater from multiple sources has surged due to economic development and increasing social demands³. Lead is highly toxic element that persists in the environment without undergoing significant degradation. Once introduced into the environment, it can be adsorbed by plants, leading to significant accumulation within their tissues. Excessive lead uptake disrupts cellular structures, leading to physiological damage, impaired growth and in severe cases plant death⁴. Furthermore, lead can enter the human body through various pathways, including ingestion of contaminated water, air, food, and skin contact. Once absorbed, lead accumulates within the body posing significant health risks⁵. Therefore, it is essential to implement effective wastewater treatment strategies to address these challenges⁶. The primary techniques for remediating lead-contaminated wastewater include chemical precipitation, ion exchange, membrane filtration, and adsorption. Among these, adsorption is widely regarded as a highly effective method due to its simplicity and efficiency in removing pollutants. However, the high cost of adsorbents limits their use in treating heavy metal-contaminated wastewater. As a result, current research is largely focused on developing advanced adsorbent materials that are not only highly efficient but also cost effective and environmentally sustainable⁷.

Polymer-based nanocomposites have attracted significant attention across diverse scientific and technological domains due to their superior and tunable properties⁸. These advanced materials have demonstrated immense potential in a broad spectrum of applications, including water purification, photovoltaic systems, wastewater remediation, electronic devices, tissue engineering scaffolds, wound dressings, antimicrobial agents, drug

¹Faculty of Material Science and Engineering, Jimma Institute of Technology, Jimma University, Jimma, Ethiopia.

²Interdisciplinary Centre for Water Research (ICWaR), Indian Institute of Science, Bangalore 560012, India.

³Environmental Science and Industrial Development Department, Faculty of Postgraduate Studies for Advanced Sciences, Beni-Suef University, Beni Suef, Egypt. ⁴Civil Engineering Department, College of Engineering, King Khalid University, Abha 61421, Saudi Arabia. ✉email: foluemm@gmail.com; praveen@iisc.ac.in

delivery platforms, and electromagnetic interference shielding systems⁹. Among conductive polymers, polyaniline (PANI) stands out due to its unique combination of cost-efficiency, high polymerization efficiency, exceptional stability, and versatility. Commonly referred to as aniline black, PANI exists in various oxidation states, enabling its adaptability for specific applications¹⁰.

Copper oxide nanoparticles (CuO NPs) are highly versatile, having applications in electrical sensors, plant disease management, field emission, and catalysis. When incorporated into nanocomposite polymers, CuO serves as an active site for adsorption due to its high surface area and strong interactions with adsorbates, thereby significantly enhancing the overall adsorption capacity. The combination of CuO with polyaniline (PANI) generates a synergistic effect that not only improves adsorption performance but also enhances the structural stability of the composite, making it more durable and resistant to degradation during adsorption-desorption cycles. Common methods for synthesizing such nanocomposites include the reduction of metals into polymers, *in situ* polymerization of monomers in the presence of metal nanoparticles, and mechanical blending of polymers with nanoparticles.¹¹.

Conventional techniques for synthesizing nanomaterials often pose significant environmental challenges due to the generation of toxic by-products. Green nanoparticles made from plant extracts have gained interest due to their safety and eco-friendliness¹². The efficacy of these green nanoparticles in wastewater treatment is attributed to the physio-chemical features exhibited by plants¹³. Green synthesis techniques utilize plant extracts to mitigate the harmful effects of conventional methods that release by-products into the environment¹⁴. Researchers have developed various nanoparticles using techniques such as thermal reduction, microwave irradiation, chemical vapor deposition, photochemical, and electrochemical methods. However, these approaches often involve harsh chemicals, leading to environmental concerns and increased costs¹⁵.

In recent times, various nanocomposite materials derived from polymers, such as PANI-ZnO, Fe₃O₄-SBCTA, Fe₃O₄-PANI-MnO₂, PMMA-boehmite, PPy-Fe₃O₄, PTh-Al₂O₃, and PVA-ZnO, have been employed for the purpose of removing Cr⁶⁺, Fe³⁺, Hg²⁺, Ar³⁺, Cu²⁺, Co²⁺ and Pb²⁺ from wastewater. Polymers exhibit a favorable surface area-to-volume ratio, enhancing their effectiveness when combined with other materials to form composites¹⁶⁻²².

The current research focuses on developing an Pb (II) adsorbent by incorporating green copper oxide nanoparticles (CuO NPs) encapsulated in polyaniline (PANI). The g-CuO NPs were obtained from the stem extract of *Haldinia cordifolia*. The resulting composite material was employed for the adsorption of Pb (II) ions and characterized using multiple analytical techniques: X-ray diffraction (XRD), scanning electron microscopy with energy dispersive X-ray spectroscopy (SEM-EDX), Fourier transform infrared spectroscopy in attenuated total reflectance mode (FTIR-ATR), X-ray photoelectron spectroscopy (XPS), Raman spectroscopy, and Brunauer-Emmett-Teller (BET) analysis. Additionally, the study investigated the influence of various parameters on adsorption efficiency, including pH, initial Pb (II) concentration, and CuO/PANI dosage. Optimization of these parameters provided insights into the adsorption mechanism and enhanced the Pb(II) removal efficiency of the composite material.

Materials and methods

Chemicals

Pb (NO₃)₂ (> 99%) and CuSO₄ (99% purity) were procured from Merck Bangalore Karnataka and used as such without any purification. APS (ammonium per sulphate) (99.9% purity) was obtained from SRL, Chemicals Ltd. Aniline (\geq 99.5%) and HCl (37%) were purchased from Spectrochem Karnataka, India.

Synthesis of g-CuO NPs

In this study, g-CuO NPs were synthesized from plants using a reported study in a previous with some modifications²³. Before extraction, the stem bark of *Haldinia cordifolia* is typically washed with deionized (DI) water. The stem part of the plant is then dried at 30 ± 2 °C. Subsequently, 5 g of *H. cordifolia* stem are ground to a fine powder, dissolved in 100 mL of DI water, and heated for 30 min at 80 ± 2 °C on a hot plate. This mixture is then filtered using a muslin cloth and filter paper. To synthesize green CuO (g-CuO) nanoparticles, 75 mL of a 0.01 M CuSO₄ solution is added to 5 mL of the *H. cordifolia* plant extract in 250 mL conical flasks, as illustrated in Supplementary Fig. S (1). These solutions are stirred for 60 min at 90 ± 2 °C at 4000 rpm on a magnetic stirrer. The precipitate is then collected by centrifugation at 8000 rpm for 10 minutes and repeatedly washed with deionized (DI) water to ensure the removal of residual impurities and obtain a high-purity product..

Synthesis of g-CuO/PANI nanocomposite

The g-CuO/PANI nanocomposite was synthesized by the *in-situ* composite formation, incorporating some modifications from the previous report²⁴. First, 0.2 g of green-synthesized CuO nanoparticles (g-CuO NPs) powder was mixed with 30 mL of a 1 M HCl. The mixture was then subjected to ultrasonic waves for 30 min to ensure uniform dispersion. Subsequently, 50 μ L of distilled aniline was added to the solution and further dispersed ultrasonically for another 30 min. In a separate beaker, 0.1675 g of ammonium persulfate (APS) was dissolved in 15 mL of 1 M HCl, and this solution was added dropwise to the first mixture, as depicted in Supplementary Fig. S (2). The resulting solution was then kept in an ice bath at 5–7 °C for 6 h with continuous stirring, and then washed with DI and ethanol. The final product, the g-CuO/PANI nanocomposite, was dried overnight in a vacuum oven at 60 °C. Pristine polyaniline (PANI) was synthesized following the same procedure as for the composite.

Characterization techniques

FTIR measurement were performed using Bruker Tensor II instrument to identify the functional groups present in CuONPs, PANI, CuO/PANI, and CuO/PANI after Pb (II) adsorption. The spectra was recorded at a resolution

of 4 cm^{-1} over the wavenumber number of $4000\text{--}500\text{ cm}^{-1}$. XRD analysis was performed using a Bruker D8 Advance, which emitted Cu K α radiation with a wavelength of 1.541 \AA . The chemical composition and electronic state of materials were studied using XPS to obtain the characteristic binding energy using Thermo K-alpha, Al anode. The morphology of g-CuO NPs, PANI, CuO/PANI, and CuO/PANI after Pb (II) adsorption was also studied using SEM-EDS (Zeiss ULTRA 55 Field Emission). For pore size and surface area analysis, the BELSORP MAX II instrument was used. This multifunctional tool evaluates vapour adsorption, chemisorption, and specific surface area/pore size distribution. Raman spectroscopy (Model-STR-300; Make-Seki Technotron Crop, Japan) was utilized to examine molecular information before and after the adsorption.

Adsorption experiments

The adsorption experiments were conducted in batch mode to evaluate the performance of the CuO/PANI composite under various conditions. A known amount of CuO/PANI was added to 100 mL Erlenmeyer flasks containing $\text{Pb}(\text{NO}_3)_2$ solutions, and the mixtures were stirred at 200 rpm to determine optimal parameters such as pH, composite dosage, and initial Pb(II) concentration. A stock solution of Pb(II) (1000 mg L^{-1}) was prepared, and desired concentrations were obtained by diluting this stock solution with deionized water. For the experiments, 100 mL of Pb(II) solutions at varying concentrations were treated with 25 mg of CuO/PANI and shaken at 200 rpm. The lead concentrations were measured before and after the adsorption process. The effects of key factors, including Pb(II) concentration, CuO/PANI dosage, and solution pH, on adsorption efficiency were systematically investigated. The removal efficiency was calculated using Equation 1.

$$\% \text{ Removal} = \left(\frac{C_O - C_t}{C_O} \right) 100 \quad (1)$$

where C_t and C_O are the final and initial concentrations.

To investigate the adsorption kinetics models, five adsorption models (intraparticle diffusion (IPD), Pseudo-first-order (PFO), Pseudo-second-order (PSO), mixed first and second order (MFSO), and Avrami) were investigated for the adsorption of Pb (II). Adsorption isotherms play a crucial role in investigating the mechanism and affinity of adsorption towards Pb (II)²⁵. Different models, namely Langmuir, Freundlich, Langmuir-Freundlich, Sips, Toth, Redlich-Peterson, Dubinin-Radushkevich, Khan, Baudu, and Fritz-Schlunder models, were used to analyze the experimental data of Pb (II) adsorption onto CuO/PANI composite.

Result and discussion

XRD diffraction studies

Figure 1 illustrates the XRD graph of the g-CuO NPs, PANI, g-CuO/PANI nanocomposite, and after Pb (II) adsorption. The XRD graph of pristine PANI shows two broad peaks at about 20° and 25° , as shown in Fig. 1a. These peaks associated to the (020) and (200) planes of PANI matched with JCPDS card No 53-1891²⁶ suggesting that PANI is semi-crystalline in nature²⁷. As shown in Fig. 1b, the XRD pattern of g-CuO nanoparticles has sharp peaks, indicating the nanoparticle's high crystallinity. The g-CuO NPs exhibit two characteristic peaks at 35° and 38° with hkl value of the (-111) and (111) planes respectively, along with multiple smaller peaks at

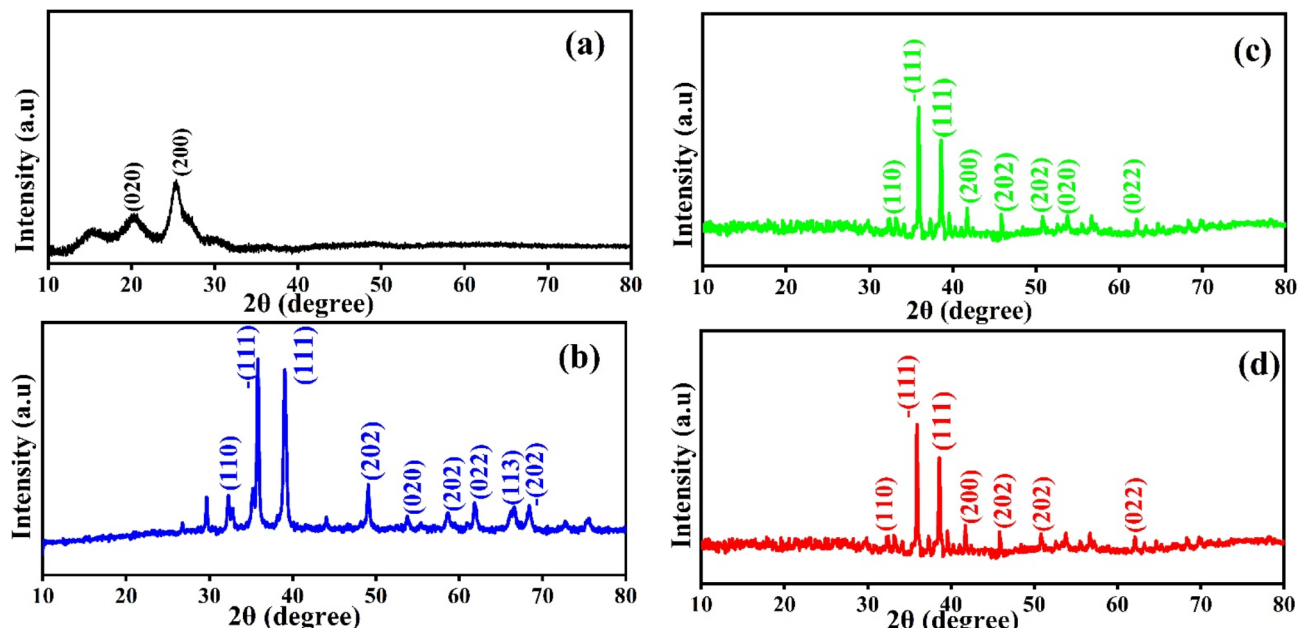


Fig. 1. XRD of (a) PANI, (b) g-CuO NPs, (c) g-CuO/PANI, and (d) g-CuO/PANI after adsorption.

higher 2θ values (32, 49, 53, 58, 61, and 68°) which correspond to the hkl (110, 202, 020, 202, 022, -202) planes respectively, JCPDS card no. 48-1548 which align with the findings of prior work with chemical synthesis routes^{28,29}. The average crystallite size of g-CuO NPs was calculated by Scherer's formula given by an equation: $D = 0.9\lambda / \beta \cos\theta$, where D is the average crystalline size of the nanoparticle, β is the FWHM of significant peaks, θ is the Bragg's angle, and λ is the wavelength of Cu K α ³⁰. The average crystallite size was observed to be of g-CuO NPs to be 17.91 nm. The XRD result of the g-CuO/PANI nanocomposite is also depicted in Fig. 1c. The nanocomposite shows a diffraction peak at 32, 35, 38, 41, 45, 50, 53, and 62°, where some peaks in pristine g-CuO NPs disappear and shifted to high 2θ value with low intensity^{31,32}. This is due to the interaction between PANI and the g-CuO nanoparticles during the formation of the nanocomposite and the semi-crystalline nature of PANI. Despite this interaction, all the characteristic CuO peaks were still visible. XRD analysis was also performed on the nanocomposite after the adsorption of lead ion. The results indicated no significant shift in the 2θ degrees, with the patterns remaining almost identical to those of the nanocomposite before adsorption, except for changes in intensity, as shown in Fig. 1d.

FTIR studies for functional groups

Fourier Transform Infrared (FTIR) spectroscopy was employed to identify the functional groups in PANI, g-CuO NPs, CuO/PANI, and CuO/PANI after Pb(II) adsorption within the wavenumber range of 500–4000 cm⁻¹ in Fig 2. For PANI, characteristic absorption bands were observed at 3438, 3280, 1580, 1490, 1346, 1143, 823, and 759 cm⁻¹ in figure 2 (a). The broad bands at 3438 cm⁻¹ and 3280 cm⁻¹ correspond to O-H and N-H stretching vibrations, respectively. The peaks at 1580 cm⁻¹ and 1490 cm⁻¹ are attributed to the C=C stretching of the quinoid and benzenoid rings, respectively³³. The bands between 1346 cm⁻¹ and 1143 cm⁻¹ are associated with C-N bending vibrations of secondary aromatic amines³⁴. Additionally, the benzenoid group exhibited C-H sp³ stretching and C=C stretching vibrations at 2998 cm⁻¹ and 1436 cm⁻¹, respectively. The quinonoid ring in PANI showed an absorbance band at 1020 cm⁻¹, while the band at 823 cm⁻¹ was attributed to C-H bonds³⁵. For g-CuO NPs, as shown in Fig. 2 (b), a broad peak near 3435 cm⁻¹ corresponds to O-H stretching vibrations, and a sharp peak at approximately 1637 cm⁻¹ is indicative of C=O stretching vibrations. The characteristic Cu-O stretching vibrations were observed at 590 cm⁻¹ and 830 cm⁻¹, confirming the presence of CuO^{36,37}.

The FTIR spectra of the (CuO/PANI) nanocomposite are different from those of pure g-CuO NPs and PANI because the peak intensity changed, and the wavenumber shifted. This can be seen in Fig. 2 (c). Absorbance peaks at 1484 and 1570 cm⁻¹ are assigned to C=C and C=N stretching mode vibration for benzenoid & quinoid

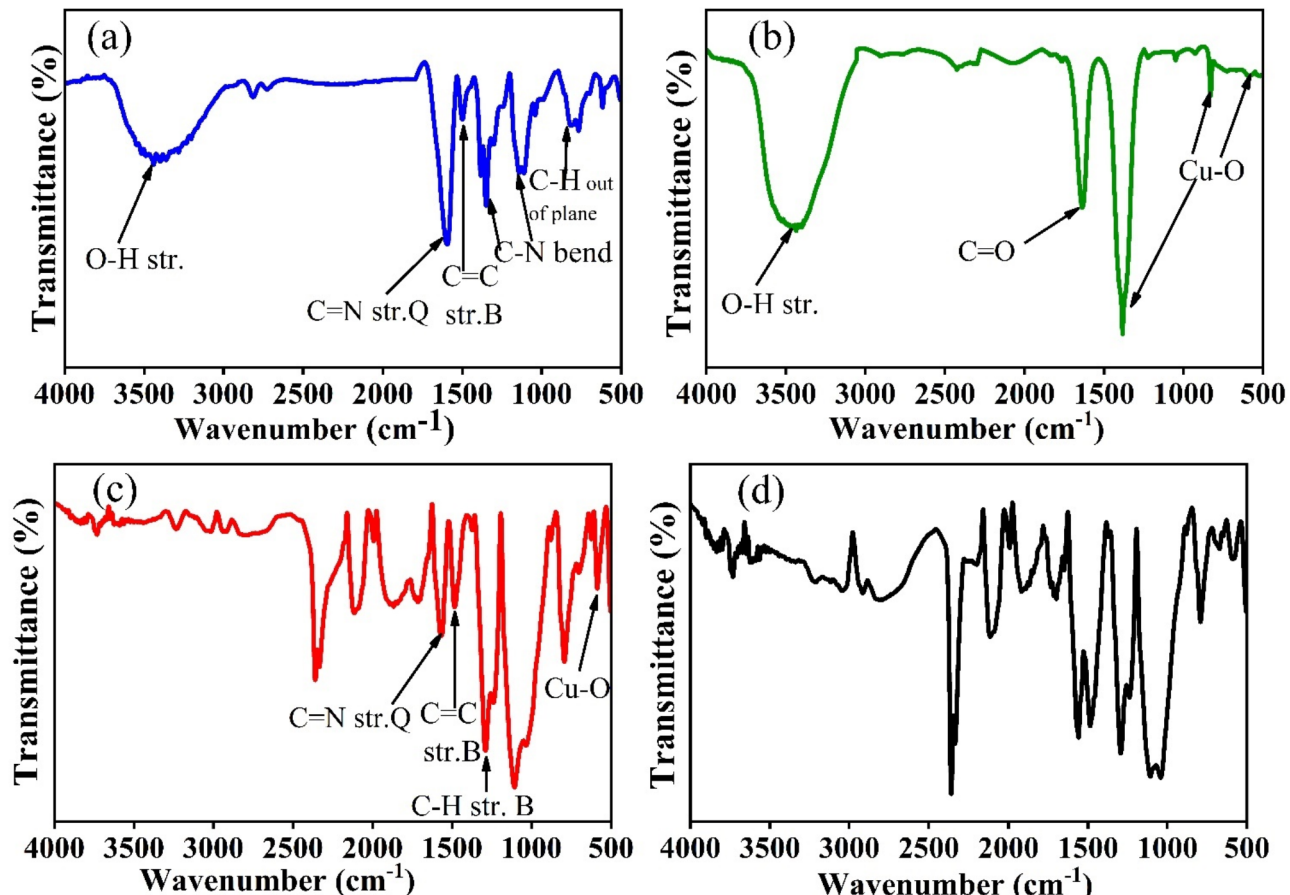


Fig. 2. FTIR of (a) PANI, (b) g-CuO NPs, (c) g-CuO/PANI, and (d) g-CuO/PANI after adsorption.

of PANI, respectively, which shows some shift in peak position and peak intensity compared to pure PANI^{38,39}. The peak that appeared at 1295 cm⁻¹ corresponds to the C-H stretching of the benzenoid ring. The peak at 586 cm⁻¹ observed in nanocomposite shows some red shift compared to g-CuO NPs, which corresponds to Cu-O stretching vibration³⁹. The shift in PANI and g-CuO, characteristic peaks in composites, indicates an interaction between them. As illustrated in Fig. 2 (d), the FTIR spectra after Pb (II) adsorption differ from those taken before adsorption in terms of peak position and intensity. The absorption peak corresponding to C=C and C=N stretching mode vibration for the benzenoid and quinonoid rings at 1484 and 1570 cm⁻¹ shifted to 1487 and 1559 cm⁻¹, a blue and red shift, respectively, and shows a more intense peak. The peak at 586 cm⁻¹, due to the Cu-O vibration bond, is shifted to 589 cm⁻¹ and shows little broadness compared to CuO/PANI nanocomposite before adsorption. These changes occur because of an interaction between the nanocomposite and Pb (II), which forms some complexes.

Surface area and pore analysis

Fig. S (3) shows the BET surface area, pore volume, and pore size of the CuO/PANI nanocomposite before and after Pb adsorption. The BET study revealed an overall decrease in surface area from 17.105 to 12.217 m² g⁻¹ following the adsorption of Pb, as shown in Table S (1). The fact that the surface area has shrunk further supports the idea that Pb ions are adsorbing into the nanocomposite material. The CuO/PANI nanocomposite's isotherm shows that it absorbs less nitrogen at low pressures, then slowly more at higher pressures until it reaches its limit. It is possible to make the adsorbent better at absorbing substances by giving it a lot of surface area and making pores of different sizes, from small micropores to larger mesopores⁴⁰.

Morphology and elemental analysis studies

The SEM image for g-CuO NPs, CuO/PANI nanocomposite, and the nanocomposite material after adsorption was carried out by Zeiss ULTRA 55 FESEM. From the SEM result of g-CuO NPs in Fig. 3 (a), it is observed that the surface morphology of the finely dispersed nanoparticles. The SEM image of the CuO/PANI nanocomposite shows a significant effect on morphology after PANI is incorporated into the g-CuO nanoparticle, as shown in Fig. 3 (b). Additionally, the morphology of nanocomposite after Pb (II) adsorption is depicted in Fig. 4 (c). An energy-dispersive X-ray spectrometer (EDS) was also conducted for the elemental analysis. As shown in Fig. 3 (a) and (b), there is a significant decrease in the weight (%) of the Cu element after nanocomposite (CuO/PANI) is formed; this may be due to the incorporation of PANI during in-situ polymerization. Moreover, the EDS of CuO/PANI in Fig. 3 (b) shows C, N, O, and Cu elements, in which the presence of N indicates aniline monomer is polymerized to PANI and interacts with g-CuO NPs. After the lead ion adsorbed, the EDS of nanocomposite has Pb in addition to the elements present in CuO/PANI nanocomposite, as shown in Fig. 3 (c).

X-ray photoelectron spectroscopy studies

XPS of CuO/PANI was carried out before and after adsorption, and Fig. 5a, b show the results. The survey spectra showed the presence of Cu1s, O1s, C1s, and N1s, which is consistent with the EDX result, as shown in Fig. 3a–c. The presence of N1s and C1s suggests the incorporation of PANI into g-CuO NPs during in-situ polymerization reactions. Fig. S (4b) shows that after C1s deconvolution, there are three peaks at 282.75, 286.23, and 290.15 eV. These correspond to C-Cu, C=C/C-C, and O-C=O, interaction between carbon atoms in the polyaniline (PANI) matrix and the copper (Cu) atoms in the CuO nanoparticles in line with previous reports⁴¹. The base peak at 934.80 eV corresponds to Cu 2p_{3/2} and 954.44 eV to Cu 2p_{1/2}, as shown by the deconvoluted peak of Cu 2p in Fig. S (4c)⁴¹. As shown in Fig. S (4c), the satellite peak at 943.31 eV indicates that Cu is in the Cu (II) form, which is characteristic of CuO and is consistent with previous work^{42,43}. Furthermore, Fig. S (4d) illustrates the deconvolution of the O1s into three peaks: 529.41 eV (O-Cu), 531.67 eV (O=N), and 532.92 eV (C-O)⁴⁴. Two peaks are also observed for N1s at 399.83 and 401.32 eV, attributed to -NH and positively charged N atoms respectively, as depicted in Fig. S (4a)⁴⁵. Figure 5 also displays the XPS spectra following Pb (II) adsorption. The survey scan spectrum after adsorption confirms the incorporation of a Pb ion into our nanocomposite, as depicted in Fig. 5. The characteristic peaks of Pb 4f for Pb (II) are observed at 139.25 and 144.14 eV, which are belonged to Pb 4f_{7/2} and Pb 4f_{5/2}, respectively, after deconvolution, as shown in Fig. S (4e)⁴⁶. The XPS result after lead ion adsorption reveals that Pb⁴⁺ is responsible for the binding energy peaks at 141.08 eV and 138.43 eV, while Pb (II) is at 138.69 eV and 143.78 eV⁴⁷. After adsorption, the survey scan shows a peak shift of C1s (284.96 eV to 285.04 eV), N1s (401.60 eV to 399.83 eV), and O1s (532.99 eV to 533.01 eV).

Raman spectroscopy studies

The Raman spectra of CuO/PANI and CuO/PANI after Pb (II) adsorption nanocomposites are depicted in Fig. S (5). For CuO/PANI nanocomposite, Fig. S (5a), the peak observed at 421 cm⁻¹ is attributed to the A_g mode, while the peaks appeared at 538 and 787 cm⁻¹ were B_{1g} and B_{2g} modes of CuO respectively. The Raman peak at 1590 cm⁻¹ is the C=C of PANI's quinonoid ring (Q), while the peak at 1501 cm⁻¹ is the C-C of the benzenoid ring (B) of PANI. The peaks at 1562 and 1412 cm⁻¹ are PANI's N-H and C=N stretching, respectively. The peaks observed at 1178 and 1268 cm⁻¹ are also belonged to the C-H and C-N bonds, respectively^{47–50}. The peaks related to PANI are visible compared to CuO; this may be due to their composite proportion. After adsorption, some peaks are shifted, and their intensities are also changed. CuO/PNI nanocomposite: after Pb (II) adsorption, the peak at 1178 cm⁻¹ (C-H) was shifted to 1166 cm⁻¹. The quinonoid ring's C=C peak nearly occupies the same Raman shift position. Moreover, the peak that is associated with the C-C of the benzenoid ring at 1501 cm⁻¹ is shifted to 1490 cm⁻¹, and a more intense peak is observed, as shown in Fig. S (5b).

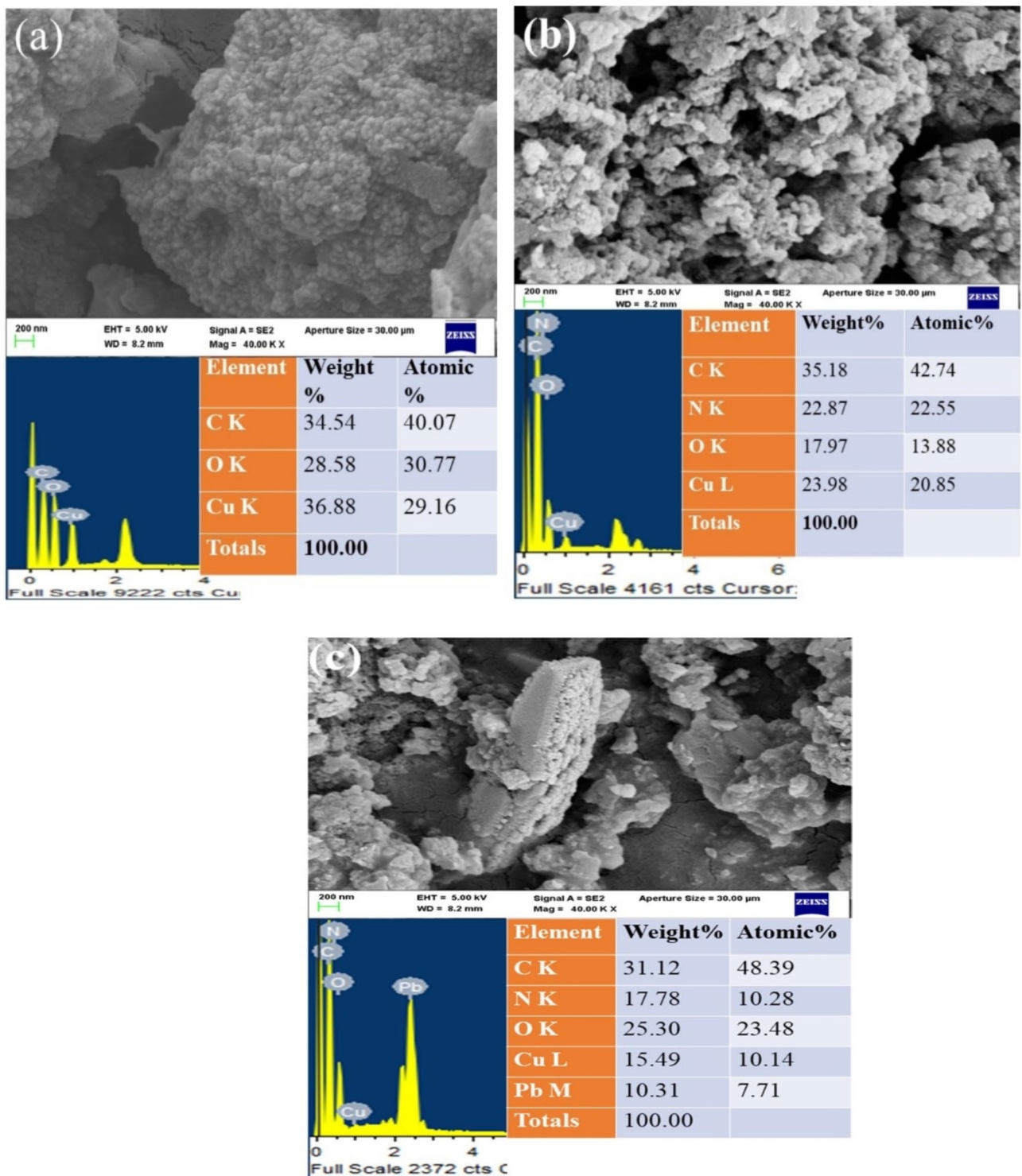


Fig. 3. SEM image and EDS spectra of (a) CuO NPs, (b) CuO/PANI nanocomposite, and (c) CuO/PANI after Pb adsorption.

Optimization study

pH variation

The pH is one factors that significantly influence the adsorption⁵¹. To check the effect of pH variation, studies were carried out with a pH range of 2 to 6, with initial ion concentration of 25 mg/L, and a CuO/PANI dosage of 25 mg/L. Figure 6 (a) shows how pH influences the removal of Pb (II). It showed a progressive increase in the removal of Pb (II) with removal percentage of 48.16 to 95.25%, when pH was increased from 2 to 6. When the pH rises above 6, lead ions precipitate as hydroxides, and removal efficiency decreases⁵². Consequently, the

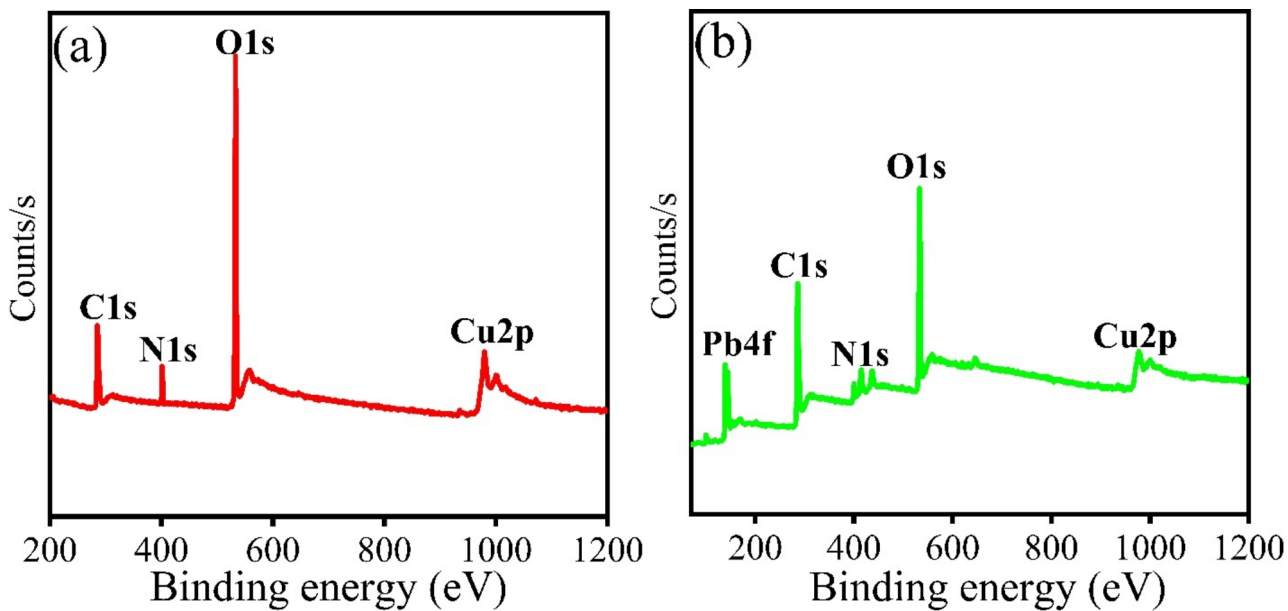


Fig. 4. Fitting of the experimental data for non-linear IPD, PFO, PSO, MFSO, and Avrami for the arrays results at different initial ion concentrations: 25 (a), 50 (b), 75 (c), 100 (d), 125 ppm (e) and linear plot of IPD (f).

adsorption percentage of Pb (II) diminished as pH increased. Following previous studies, the results demonstrate that the adsorption efficiency decreases at pH levels greater than 6. The maximum adsorption was achieved at pH = 6, decreasing significantly when the pH > 6. This finding aligns with previously reported research, further supporting our experimental observations and the point of zero change (PZC) shown in Fig. S(6)⁵³.

Dosage variation

The effect of adsorbent dosage on Pb(II) ion removal was investigated using dosages of 25, 50, 75, 100, and 125 mg L⁻¹. As the CuO/PANI nanocomposite dosage increased, the Pb(II) removal efficiency improved; however, the adsorption efficiency began to decrease at higher dosages⁵⁴. This trend can be attributed to the increased concentration of the composite, which leads to a higher dosage and a reduced overall surface area available for adsorption of Pb(II) removal increased with the adsorbent dosage until a saturation point was reached, as depicted in Fig. 6(b)⁵⁵. This indicates that additional active sites participate in the adsorption process until all available sites are fully occupied by the adsorbent.

Initial ion concentration variation

Figure 6(c) depicts the effect of varying initial ion concentration of Pb (II) (from 25 to 125 ppm). As the initial ion concentration of Pb (II) increases, the CuO/PANI composite becomes better at adsorbing it, going from 96 to 295.73 mg g⁻¹. Many Pb (II) molecules were competing for an available adsorption site on the CuO/PANI, making it less able to hold molecules. As the starting concentrations grow, the absorption capacity rises, but the adsorption percentage falls due to surface saturation⁵⁴.

Adsorption Kinetics

To investigate the adsorption kinetics models, five adsorption models (intraparticle diffusion (IPD), Pseudo-first-order (PFO), Pseudo-second-order (PSO), mixed first and second order (MFSO), and Avrami) were investigated for the adsorption of Pb (II) at five initial concentrations (25, 50, 75, 100 and 125 mg/L) over time at pH 2 and dose 25 mg/L. It can be seen the maximum adsorption capacities increase as the initial concentrations of Pb (II) also increase. The adsorption of Pb (II) ions at 25, 50, 75, 100, and 125 ppm onto CuO/PANI show fast adsorption, with the corresponding removal efficiencies 29.3%, 23.78%, 14.3%, 11.8% and 10.9% in the first 30 min. This was followed by a lower removal rate of up to 240 min, and finally, the adsorption achieved the equilibrium phase at 210 min (Fig. 4a–e). The maximum adsorption capacities are 90.86, 171.04, 143.62, 256.39 and 322.844 mg/g, which are corresponding to removal efficiencies of 96.3%, 72.6%, 66.7%, 62.6%, and 59.1%, for the initial Pb (II) concentrations of 25 ppm (Fig. 4a), 50 ppm (Fig. 4b), 75 ppm (Fig. 4c), 100 ppm (Fig. 4d) and 125 ppm (Fig. 4e), respectively.

The fitting of the kinetic models for the Pb (II)@CuO/PANI adsorption system is evaluated based on the agreement of the calculated and experimental adsorption values and the correlation coefficient values. From Fig. 4; Table 1, it can be confirmed that both PFO Avrami models can describe the data at all concentrations of Pb (II) with high correction coefficients ($0.97 < R^2 < 0.99$). Although PSO and MFSO models yield high correlation coefficients ($0.97 < R^2 < 0.99$), both models can't be used to describe Pb (II)@ CuO/PANI adsorption system since the predicted values of the q_{\max} are higher than the calculated one. For the IPD model, there is no agreement between the experimental and the calculated data; in addition, the value of c_{ip} is equal to zero for all

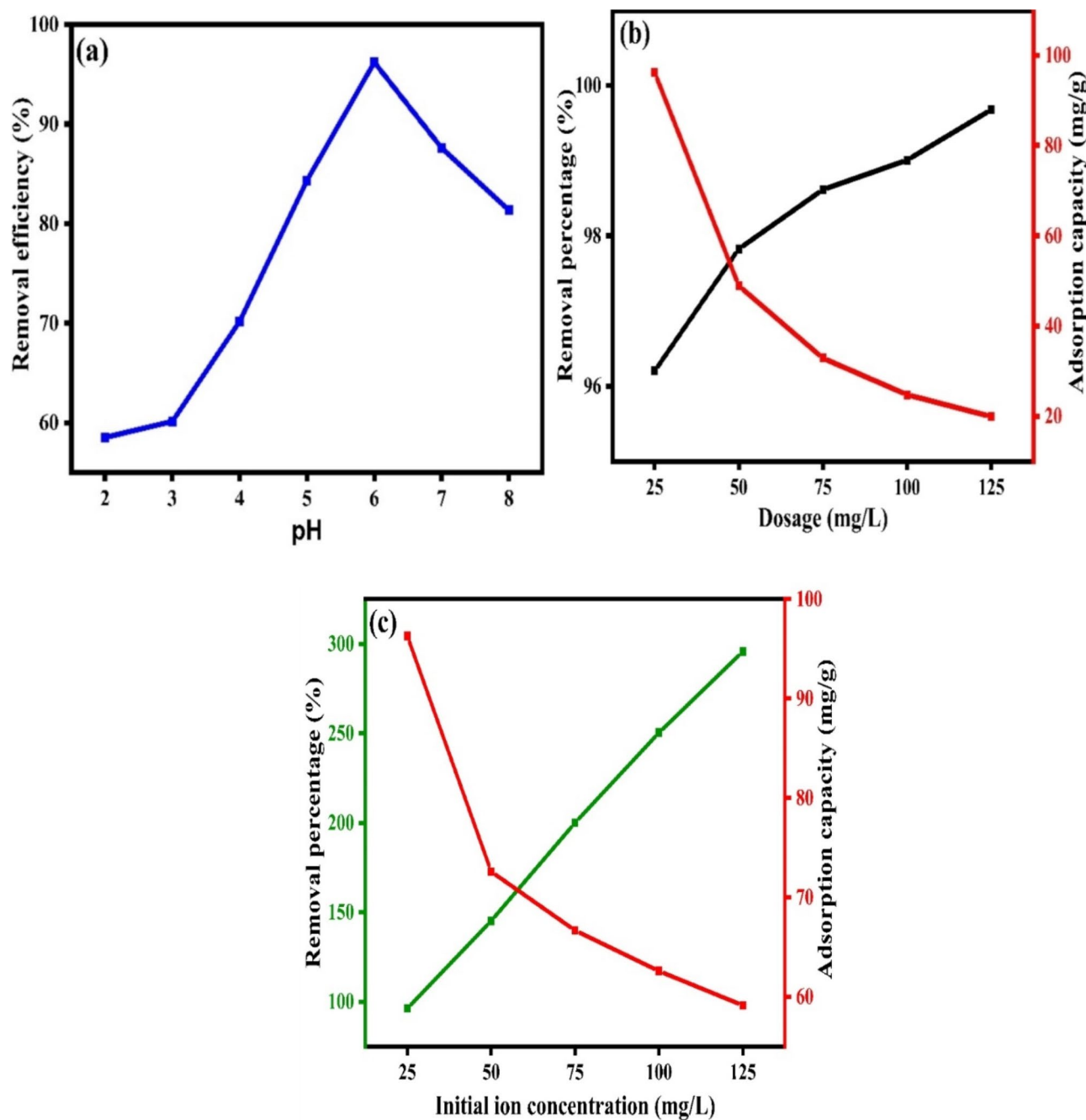


Fig. 5. XPS spectra of CuO/PANI nanocomposite (a) before and (b) after Pb (II) adsorption survey scan.

concentrations under study, which means that the non-linear form is converted to the linear form ($q_t = k_{ip} \sqrt{t}$). So, the linear form is further investigated, as shown in Fig (e). The results show that fitting the adsorption data of Pb (II) onto CuO/PANI at 25, 50, 75, 100 and 125 mg/L by plotting q_t versus $t^{0.5}$ resulted in lines that don't pass through the origin, which suggests that the IPD is not only the rate-limiting step and the adsorption system may be controlled by both porous diffusion and film diffusion.

Where q_e and q_t (mg g^{-1}) are the adsorption capacity at equilibrium and time t , respectively. c_{ip} (mg g^{-1}), k_1 (min^{-1}), k_2 ($\text{gmg}^{-1} \text{min}^{-1}$), k ($\text{mg g}^{-1} \text{min}^{-1}$), and k_{av} (min^{-1}) are the IPD, PFO, PSO, MFSO, and Avrami models constants, respectively. f_2 (-) and k_{ip} ($\text{mg g}^{-1} \text{min}^{-1(1/2)}$) are the MFSO and IPD coefficients, n_{av} (-) is Avrami component.

Adsorption isotherm modeling

Adsorption isotherms play a crucial role in investigating the mechanism and affinity of adsorption towards Pb (II)²⁵. Different models, namely Langmuir, Freundlich, Langmuir-Freundlich, Sips, Toth, Redlich-Peterson, Dubinin-Radushkevich, Khan, Baudu, and Fritz-Schlunder models, were used to analyze the experimental data

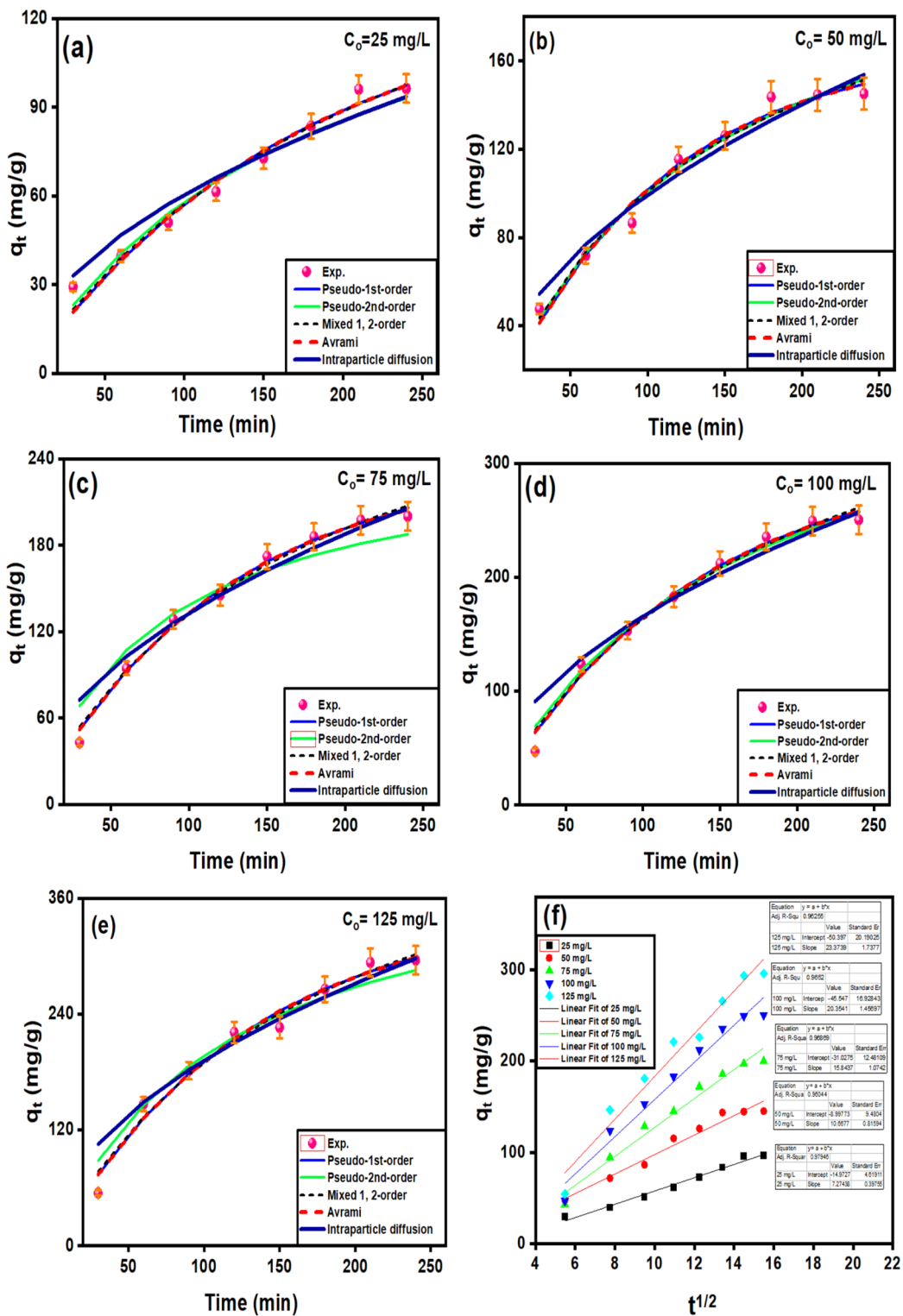


Fig. 6. Optimization studies of (a) pH, (b) dosage, and (c) initial ion concentration.

of Pb (II) adsorption onto CuO/PANI at a temperature of 298 K. The findings obtained from the non-linear models are displayed in Fig. 7a–j; Table 2.

Figure 7 shows that the adsorption capacity of CuO/PANI towards Pb (II) strongly depends on Pb's initial concentration (II). The maximum adsorption capacities (q_{\max}) of CuO/PANI to adsorb Pb (II) ions are increased (96.30, 145.16, 200.05, 250.33 and 295.74 mg/g) as C_o increase (25, 50, 75, 100 and 125 mg Pb (II) /L, respectively) as represented in Fig. 7. The correlation coefficients (R^2) values of the fitted non-linear models along with the model's parameters are shown in Table 2. Only the Freundlich model can describe the adsorption system well

Model	Parameter	C ₀ [mg/L]				
		25	50	75	100	125
PFO $q_t = q_e (1 - \exp(-k_1 t))$	q _{exp} [mg/g]	96.30	145.16	200.05	250.33	295.74
	K ₁ [min ⁻¹]	0.0058	0.0094	0.0083	0.0078	0.0078
	q _e [mg/g]	128.77	166.77	237.24	304.60	352.38
	R ² [-]	0.97	0.98	0.99	0.99	0.98
PSO $q_t = \frac{k_2 q_e^2 t}{1 + k_2 q_e t}$	K ₂ [g/mg.min]	3.36E-05	3.16E-05	6.08E-05	1.56E-05	2.11E-05
	q _e [mg/g]	163.61	236.451	236.45	419.70	419.71
	R ² [-]	0.97	0.98	0.90	0.98	0.96
	K [mg.g ⁻¹ .min ⁻¹]	0.0004	0.0003	0.0003	0.0002	0.0002
MFSO $q_t = q_e \frac{1 - \exp(-kt)}{1 - f_2 \exp(-kt)}$	q _e [mg.g ⁻¹]	185.30	229.62	339.84	444.15	512.00
	f ₂ [-]	0.899	0.960	0.953	0.962	0.967
	R ² [-]	0.98	0.98	0.99	0.98	0.98
	q _e [mg/g]	128.67	166.77	237.24	304.57	352.37
Avrami $q_t = q_e [1 - \exp(-k_{av} t)^{nav}]$	k _{av} [min ⁻¹]	0.079	0.100	0.094	0.091	0.091
	n _{av} [-]	0.075	0.095	0.088	0.086	0.086
	R ² [-]	0.97	0.98	0.99	0.99	0.98
	k _{ip} [mg/g.min ^{1/2}]	6.04	9.92	13.28	16.58	19.21
IPD $q_t = k_{ip} \sqrt{t} + c_{ip}$	c _{ip} [mg/g]	0	0	0	0	0
	R ² [-]	0.95	0.96	0.95	0.93	0.93

Table 1. Different kinetic models for the adsorption of pb (II) onto CuO/PANI.

with a high R² value, and the value of (1/n)<1 suggests that the adsorption process is favourable. Langmuir, Dubinin–Radushkevich and Baudu models failed to predict the kinetic of the Pb (II)@CuO/PANI adsorption since the calculated q_{max} are higher than the experimental one in addition to the corresponding low values of R² (0.73, 0.62, and 0.73 respectively). Although Langmuir-Freundlich, SiPs, Toth and Redlich-Peterson represent high values of R² Table 2, the calculated q_{max} according to these models is far from the experimental one. Also, both of Fritz-Schlunder and Khan models failed to describe the Pb (II)@CuO/PANI adsorption system since the predicted values of q_{max} are much less than the experimental one, even with the corresponding high values of R².

Where: q_e (mg g⁻¹) is the amount of Pb(II) adsorption at equilibrium, C_e is the equilibrium concentration of Pb(II) in solution, q_{max} (mg g⁻¹) is the maximum adsorption capacity, K_L (L mg⁻¹) is Langmuir isotherm constant, K_{LF} is the equilibrium constant for heterogeneous solid, K_F (L mg⁻¹) and n are the coefficients related to adsorption capacity and strength constants of the Freundlich isotherm model, respectively, and K_{LF} is a heterogeneous parameter, and it lies between 0 and 1, k_s is Sips isotherm constant; ns is the Sips isotherm model exponent also known as heterogeneity factor, K_R and a_R are the Redlich-Peterson constants; β_R is the exponent that can be lied between 0 and 1, K_T (mg g⁻¹) is the constant, a_T (mg L⁻¹) is Toth constant, z refers to the degree of heterogeneity of the adsorption systems, while m₁, m₂, K₁, and K₂, are the Fritz-Schlunder parameters.

Comparison study

The data in Supplementary Table 2 illustrate the Pb (II) Pb (II) adsorption capacity of the g-CuO/PANI adsorbent in comparsion to previously reported findings. The adsorption capacity for each adsorbent depends on various factors, including the type of pollutant, pH level, adsorption process, time, etc. The green CuO/PANI nanocomposite reported in this study exhibits high and effective adsorption capability for Pb (II).

Reusability study

The reusability of the adsorbent is crucial for ensuring a cost-effective and practical adsorption process. Sequential batch adsorption-desorption tests to determine the recycling potential of the CuO/PANI composite. The experiments involved mixing 15 mg of CuO/PANI with a 10 mg L⁻¹ solution of lead and then stirred this mixture for 6 h until equilibrium. This process was repeated a total of seven successive times as shown in Fig. S(7). The first cycle showed the highest recovery percentage (98.86%) in NaOH while 88.57% in HCl medium. This suggests that the synthesized material have a remarkable regeneration ability to adsorb Pb (II) ions.

Conclusion

This study represents the green extraction of CuO nanoparticles from *Halimnia cordifolia* stem bark, which were subsequently composited with polyaniline (PANI) to fabricate an advanced green adsorbent for the removal of lead ions . Various characterization techniques, including FTIR, XRD, SEM-EDS, XPS, and Raman spectroscopy, validated the synthesis of CuO nanoparticles and the resulting nanocomposites. The synthesized nanocomposite exhibits favourable properties, such as a substantial surface area and a high Pb (II) adsorption capacity. Different parameters affecting the adsorption process were optimized, and various isothermal and kinetic models were applied to determine the interaction between the adsorbent and adsorbate, the maximum adsorption capacity (q_{max}), and the adsorption rate. The q_{max} for Pb (II) removal was determined to be 295.74 mg g⁻¹ at pH 6. The highly adsorptive nature of the g-CuO/PANI nanocomposite demonstrates its effectiveness as a nanomaterial

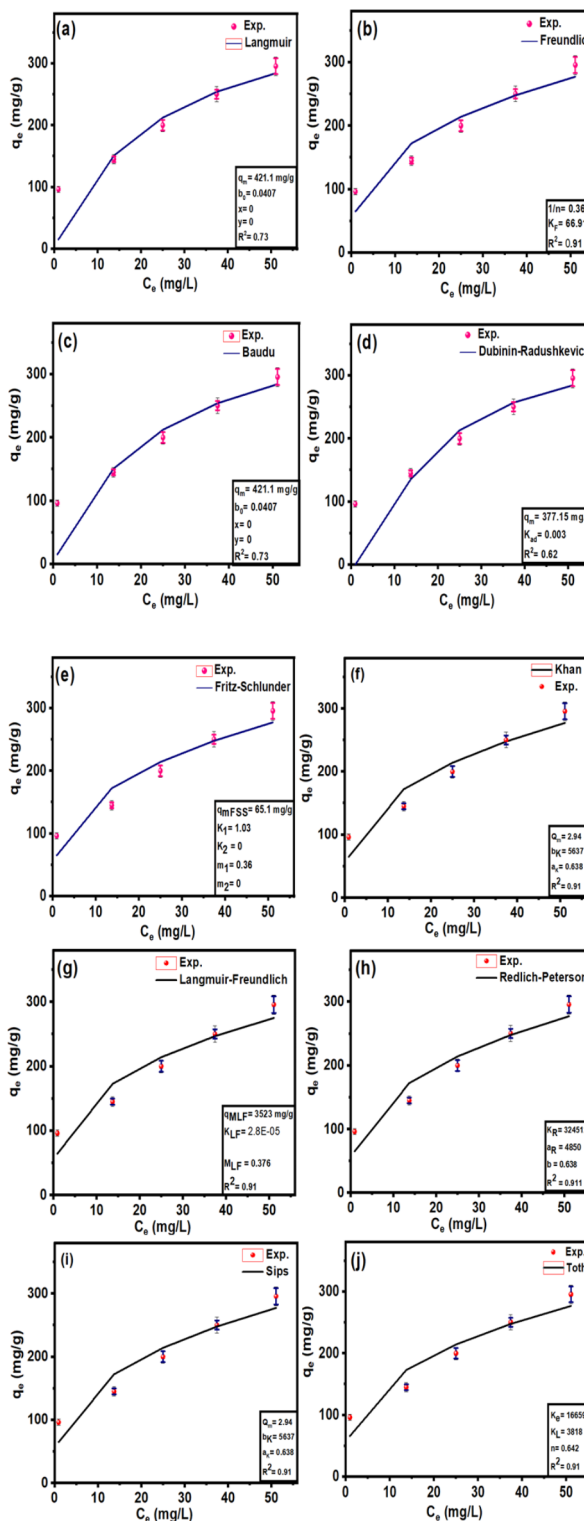


Fig. 7. Fitting of the adsorption isotherm modelling of Pb (II) at 298 K using Langmuir (**a**), Freundlich (**b**), Baudu (**c**), Dubinin–Radushkevich (**d**), Fritz-Schlunder (**e**), Khan (**f**), Langmuir-Freundlich (**g**), Redlich-Peterson (**h**), Sips (**i**), and Toth (**j**) models.

for removing Pb (II) from water. However, further research is required to confirm the nanocomposite's efficacy in removing various heavy metals and to manage the associated risks. The CuO/PANI composite exhibits strong adsorption performance and potential for reuse, making it a promising material for practical applications. However, this study is constrained by certain limitations, including a lack of detailed investigation into the underlying adsorption mechanisms and the effect of temperature on adsorption efficiency. Future research

Model	Parameter	Value	Model	Parameter	Value
Langmuir $q_e = q_{max} \frac{K_L C_e}{1 + K_L C_e}$	q_{max} (mg. g ⁻¹)	421.14	Freundlich $q_e = K_f C_e^{1/n}$	1/n	0.36
	K_L	0.041		K_f	66.91
	R^2	0.73		R^2 (-)	0.91
Langmuir-Freundlich $q_e = \frac{q_{max} (K_{LF} C_e)^{MLF}}{1 + (K_{LF} C_e)^{MLF}}$	MLF (mg. g ⁻¹)	3523	Dubinin-Radushkevich	q_m (mg. g ⁻¹)	377.15
	K_{LF}	2.8E-05		K_d	0.003
	C_e	0.377		R^2 (-)	0.62
	R^2 (-)	0.91			
Khan $q_e = \frac{q_{max} b_K C_e}{(1 + b_K C_e)^{a_K}}$	q_{max} (mg. g ⁻¹)	2.94	Sips $q_e = \frac{q_{max} K_s (C_e)^{1/ns}}{1 + K_s (C_e)^{1/ns}}$	q_{max} (mg. g ⁻¹)	281,219
	b_K	5637		K_s	0.0002
	a_K	0.638		1/n	0.3612
	R^2 (-)	0.91		R^2 (-)	0.91
Redlich-Peterson $q_e = \frac{K_R C_e}{1 + a_R C_e^{\beta R}}$	K_R	324,512	Toth $q_e = \frac{K_T C_e}{(a_T + C_e^Z)^{1/Z}}$	K_t	166,591
	a_R	4850		a_T	3818
	β	0.638		Z	0.643
	R^2 (-)	0.91		R^2 (-)	0.91
Baudu $q_e = \frac{q_{max} b_o C_e^{1+x+y}}{1 + b_o C_e^{1+x}}$	q_m (mg. g ⁻¹)	421.15	Fritz-Schlunder $q_e = \frac{q_{max} K_1 C_e^{m1}}{1 + K_2 C_e^{m2}}$	q_{mFSS} (mg. g ⁻¹)	65.09
	b_o	0.041		K_1	1.028
	x	0		K_2	0
	y	0		m_1	0.362
	R^2 (-)	0.73		m_2	0
				R^2 (-)	0.92

Table 2. The parameters of the adsorption isotherm model for Pb (II) by CuO/PANI.

should focus on addressing these gaps, as well as exploring the nanocomposite's efficacy in removing a broader spectrum of heavy metals. Such efforts will be critical in optimizing the material's performance under diverse environmental conditions and expanding its practical applicability.

Data availability

Data will be made available upon request by the corresponding author.

Received: 30 August 2024; Accepted: 2 December 2024

Published online: 28 December 2024

References

- Wu, Q. et al. Adsorption characteristics of pb (II) using biochar derived from spent mushroom substrate. *Sci. Rep.* **9**, 15999 (2019).
- Dai, X. et al. Enhanced bifunctional adsorption of anionic and cationic pollutants by MgAl LDH nanosheets modified montmorillonite via acid-salt activation. *Appl. Clay Sci.* **233**, 106815 (2023).
- Jing, C. et al. Low carbonate contaminative and ultrasmall NiAl LDH prepared by acid salt treatment with high adsorption capacity of methyl orange. *Ind. Eng. Chem. Res.* **58** (27), 11985–11998 (2019).
- Raj, K. & Das, A. P. Lead pollution: impact on environment and human health and approach for a sustainable solution. *Environ. Chem. Ecotoxicol.* **5**, 79–85 (2023).
- Collin, M. S. et al. Bioaccumulation of lead (pb) and its effects on human: a review. *J. Hazard. Mater.* **Adv. 7**, 100094 (2022).
- Qasem, N. A., Mohammed, R. H. & Lawal, D. U. Removal of heavy metal ions from wastewater: a comprehensive and critical review. *Npj Clean. Water.* **4** (1), 1–15 (2021).
- Jagadeesh, N. & Sundaram, B. Adsorption of pollutants from wastewater by biochar: a review. *J. Hazard. Mater.* **Adv. 9**, 100226 (2023).
- Fu, S. et al. Some basic aspects of polymer nanocomposites: a critical review. *Nano Mater. Sci.* **1** (1), 2–30 (2019).
- Beygisangchin, M. et al. Preparations, properties, and applications of polyaniline and polyaniline thin films—A review. *Polymers* **13** (12), 2003 (2021).
- Majeed, A. H. et al. A Review on polyaniline: Synthesis, properties, nanocomposites, and electrochemical applications. *Int. J. Polym. Sci.* **2022** (2022).
- Mousa, A. M. et al. Biosynthetic new composite material containing CuO nanoparticles produced by aspergillus terreus for 47Sc separation of cancer theranostics application from irradiated ca target. *Appl. Radiat. Isot.* **166**, 109389 (2020).
- Al-darwesh, M. Y., Ibrahim, S. S. & Mohammed, M. A. *A Review on Plant Extract Mediated Green Synthesis of Zinc Oxide Nanoparticles and Their Biomedical Applications*, 101368 (Results in Chemistry, 2024).
- Sachan, D., Ramesh, A. & Das, G. *Green Synthesis of Silica Nanoparticles from leaf Biomass and its Application to Remove Heavy Metals from Synthetic Wastewater: A Comparative Analysis*, 100467 (Environmental Nanotechnology, Monitoring & Management, 2021).
- Devi, D. et al. Eco-friendly green synthesis approach and evaluation of environmental and biological applications of iron oxide nanoparticles. *Inorg. Chem. Commun.* **110700** (2023).
- Naz, S. et al. Synthesis, biomedical applications, and toxicity of CuO nanoparticles. *Appl. Microbiol. Biotechnol.* **107** (4), 1039–1061 (2023).
- Joshi, N. C. et al. Synthesis and adsorption applications of PPY/Fe3O4 nanocomposite based material. *Nano-Structures Nano-Objects* **25**, 100669 (2021).

17. Alosaimi, E. H. et al. Adsorptive performance of tetracarboxylic acid-modified magnetic silica nanocomposite for recoverable efficient removal of toxic cd (II) from aqueous environment: equilibrium, isotherm, and reusability studies. *J. Mol. Liq.* **334**, 116069 (2021).
18. Ghamari, M. et al. Aluminum oxyhydroxide-doped PMMA hybrids powder prepared via facile one-pot method towards copper ion removal from aqueous solution. *Int. Nano Lett.* **9** (4), 317–325 (2019).
19. Joshi, N. C., Malik, N. & Singh, A. Synthesis and characterizations of polythiophene-Al₂O₃ based nanosorbent and its applications in the removal of pb 2+, cd 2+ and zn 2+ ions. *J. Inorg. Organomet. Polym Mater.* **30**, 1438–1447 (2020).
20. Salehi-Babarsad, F. et al. Heavy metal removal by using ZnO/organic and ZnO/inorganic nanocomposite heterostructures. *Int. J. Environ. Anal. Chem.* **100** (6), 702–719 (2020).
21. Xu, S. et al. Preparation of PVA/tetra-ZnO composite with framework-supported pore-channel structure and the removal research of lead ions. *Environ. Sci. Pollut. Res.* **26**, 24062–24074 (2019).
22. Zhang, J. et al. Fe 3 O 4/PANI/MnO 2 core-shell hybrids as advanced adsorbents for heavy metal ions. *J. Mater. Chem. A.* **5** (8), 4058–4066 (2017).
23. Alhalili, Z. Green synthesis of copper oxide nanoparticles CuO NPs from Eucalyptus Globoulus leaf extract: Adsorption and design of experiments. *Arab. J. Chem.* **15** (5), 103739 (2022).
24. Nagaraja, M. et al. Polyaniline-CuO nanocomposite: Electrical, structural and sensor properties. *Mater. Today Proc.* **49**, 1989–1992 (2022).
25. Kalam, S. et al. Surfactant adsorption isotherms: a review. *ACS Omega.* **6** (48), 32342–32348 (2021).
26. Vijayalakshmi, S. et al. Structural, electrical, and photocatalytic investigations of PANI/ZnO nanocomposites. *Ionics* **27**, 2967–2977 (2021).
27. Ajeeb, K. & Kareem, Q. Synthesis and characteristics of polyaniline (PANI) filled by graphene (PANI/GR) nano-films, in *Journal of Physics: Conference Series* (IOP Publishing, 2019).
28. Ansari, M. O. et al. DC electrical conductivity retention and antibacterial aspects of microwave-assisted ultrathin CuO@ polyaniline composite. *Chem. Pap.* **74**, 3887–3898 (2020).
29. Vyas, S. et al. High performance conducting nanocomposites polyaniline (PANI)-CuO with enhanced antimicrobial activity for biomedical applications. *ES Mater. Manuf.* **15**, 46–52 (2021).
30. Alam, M. W. et al. Green synthesis of Ni-Cu-Zn based nanosized metal oxides for photocatalytic and sensor applications. *Crystals* **11** (12), 1467 (2021).
31. Selvaraj, P. K., Sivakumar, S. & Selvaraj, S. Embargo nature of CuO-PANI composite against corrosion of mild steel in low pH medium. *J. Electrochem. Sci. Technol.* **10** (2), 139–147 (2019).
32. Sohail, Y. et al. Polyaniline-coated nanoparticles of zinc oxide and copper oxide as antifungal agents against aspergillus parasiticus. *Front. Plant Sci.* **13**, 925451 (2022).
33. Manuel, J., Salguero, T. & Ramasamy, R. P. Synthesis and characterization of polyaniline nanofibers as cathode active material for sodium-ion battery. *J. Appl. Electrochem.* **49**, 529–537 (2019).
34. Torosyan, M. S. & Durgaryan, N. K. Conductive polymers as materials used in sensors for determination of important volatile compounds in the field of food safety. *Proceedings of the YSU B: Chemical and Biological Sciences* **57**(3 (262)), 190–198 (2023).
35. Vadiraj, K. & Belagali, S. Characterization of polyaniline for optical and electrical properties. *IOSR J. Appl. Chem.* **8** (1), 53–56 (2015).
36. Nzilu, D. M. et al. Green synthesis of copper oxide nanoparticles and its efficiency in degradation of rifampicin antibiotic. *Sci. Rep.* **13** (1), 14030 (2023).
37. Varughese, A., Kaur, R. & Singh, P. *Green synthesis and characterization of copper oxide nanoparticles using Psidium guajava leaf extract*, in *IOP Conference Series: Materials Science and Engineering* (IOP Publishing, 2020).
38. Rahman, G., Rahman, M. U. & Najaf, Z. In situ synthesis of PANI/CuO nanocomposites for non-enzymatic electrochemical glucose sensing. *Appl. Chem. Eng.* **3** (2), 9–17 (2020).
39. Ashokan, S., Ponnuswamy, V. & Jayamurugan, P. Fabrication and characterization PANI/CuO hybrid films by nebulizer spray pyrolysis technique for diode applications. *Optik* **126** (20), 2591–2595 (2015).
40. Wilson, S. M. et al. Effect of pore size and heterogeneous surface on the adsorption of CO₂, N₂, O₂, and ar on carbon aerogel, RF aerogel, and activated carbons. *Microporous Mesoporous Mater.* **322**, 111089 (2021).
41. Jiang, J. et al. Self-supported sheets-on-wire CuO@Ni (OH) 2/Zn (OH) 2 nanoarrays for high-performance flexible quasi-solid-state supercapacitor. *Processes* **9** (4), 680 (2021).
42. Liu, R. et al. Colorimetric determination of lead (II) or mercury (II) based on target induced switching of the enzyme-like activity of metallothionein-stabilized copper nanoclusters. *Microchim. Acta* **186**, 1–8 (2019).
43. Boruban, C. & Esenturk, E. N. Activated carbon-supported CuO nanoparticles: a hybrid material for carbon dioxide adsorption. *J. Nanopart. Res.* **20**, 1–9 (2018).
44. Khan, M. A. et al. Surface study of CuO nanopetals by advanced nanocharacterization techniques with enhanced optical and catalytic properties. *Nanomaterials* **10** (7), 1298 (2020).
45. Waghmode, B. J. et al. Studies on morphology of polyaniline films formed at liquid–liquid and solid–liquid interfaces at 25 and 5 C, respectively, and effect of doping. *Colloid Polym. Sci.* **292**, 1079–1089 (2014).
46. Kang, X. et al. Modification of Ti/Sb-SnO₂/PbO₂ electrode by active granules and its application in Wastewater containing copper ions. *Catalysts* **13** (3), 515 (2023).
47. Maruthi, N. et al. Anticorrosive polyaniline-coated copper oxide (PANI/CuO) nanocomposites with tunable electrical properties for broadband electromagnetic interference shielding. *Colloids Surf. A.* **621**, 126611 (2021).
48. Nafady, A., Albaqami, M. D. & Alotaibi, A. M. CuO nanoparticles embedded in conductive PANI framework for periodic detection of alcohol from sweat. *Colloid Polym. Sci.* **301** (5), 517–526 (2023).
49. Panesar, M. J. et al. *Effect of Addition of Polyaniline (PANI) on the properties of copper (II) Oxide nanoparticles*, in *Journal of Physics: Conference Series* (IOP Publishing, 2020).
50. Sengar, M. S. et al. CuO decorated polyaniline nanocomposite-based sensor for the electrochemical determination of an opioid analgesic. *Ionics* 1–16. (2022).
51. Birniwa, A. H. et al. Cobalt oxide doped polyaniline composites for methyl orange adsorption: optimization through response surface methodology. *Case Stud. Chem. Environ. Eng.* **9**, 100553 (2024).
52. Cruz-Lopes, L. P. et al. Ideal pH for the adsorption of metal ions Cr6+, Ni2+, Pb2+ in aqueous solution with different adsorbent materials. *Open. Agric.* **6** (1), 115–123 (2021).
53. Sepehri, S. et al. Pb (II) removal from aqueous solutions by adsorption on stabilized zero-valent iron nanoparticles—a green approach. *Water* **15** (2), 222 (2023).
54. Bidhendi, M. E. et al. Removal of lead ions from wastewater using magnesium sulfide nanoparticles caged alginate microbeads. *Environ. Res.* **216**, 114416 (2023).
55. Zulfika, H. B. Z. M., Baini, R. & Zauzi, N. S. A. Effect of pH, Dosage and concentration on the adsorption of Congo red onto untreated and treated aluminium dross. in *IOP Conference Series: Materials Science and Engineering* (IOP Publishing, 2017).

Acknowledgements

Hailemariam would like to thank Jimma University, Jimma Institute of Technology, Faculty of Material Sci-

ence & Engineering and Indian Institute of Science, Department of Materials Engineering. Dr. Simranjeet Singh would like to acknowledge DBT HRD Project & Management Unit, Regional Center for Biotechnology, NCR Biotech Science Cluster, Faridabad, Haryana for Research Associateship (DBT-RA). The authors wish to express their gratitude to the Ministry of Education (MoE) for their support under the fellowship MoE-STARS/STARS-2/2023-0714, dated September 26, 2023.

Author contributions

H.A. and S.S.: Writing, reviewing, editing, and writing the original draft. N .S., and N. A .K.: Data analysis and editing. P.C.R. and FEO : Visualization, Writing, reviewing, editing, and supervision. All authors reviewed the manuscript.

Declarations

Competing interests

The authors declare no competing interests.

Additional information

Supplementary Information The online version contains supplementary material available at <https://doi.org/10.1038/s41598-024-81970-2>.

Correspondence and requests for materials should be addressed to F.E.O. or P.C.R.

Reprints and permissions information is available at www.nature.com/reprints.

Publisher's note Springer Nature remains neutral with regard to jurisdictional claims in published maps and institutional affiliations.

Open Access This article is licensed under a Creative Commons Attribution-NonCommercial-NoDerivatives 4.0 International License, which permits any non-commercial use, sharing, distribution and reproduction in any medium or format, as long as you give appropriate credit to the original author(s) and the source, provide a link to the Creative Commons licence, and indicate if you modified the licensed material. You do not have permission under this licence to share adapted material derived from this article or parts of it. The images or other third party material in this article are included in the article's Creative Commons licence, unless indicated otherwise in a credit line to the material. If material is not included in the article's Creative Commons licence and your intended use is not permitted by statutory regulation or exceeds the permitted use, you will need to obtain permission directly from the copyright holder. To view a copy of this licence, visit <http://creativecommons.org/licenses/by-nc-nd/4.0/>.

© The Author(s) 2024